Physical parameters for Orion KL from modelling its *ISO* high-resolution far-IR CO line spectrum

M. R. Lerate,[1,2]⋆ J. Yates,[1] S. Viti,[1] M. J. Barlow,[1] B. M. Swinyard,[2] G. J. White,[2,3] J. Cernicharo[4] and J. R. Goicoechea[5]

[1]*University College London, Gower Street, London WC1E 6BT*
[2]*Rutherford Appleton Laboratory, Chilton, Didcot OX11 0QX*
[3]*Department of Physics and Astronomy, The Open University, Milton Keynes MK6 7AA*
[4]*CSIC, Instituto de Estructura de la Materia, Serrano 121, 28006 Madrid, Spain*
[5]*LERMA, UMR 8112, CNRS, Observatoire de Paris and Ecole Normale Superieure, 24 Rue Lhomond 75231 Paris Cedex 05, France*

ABSTRACT

As part of the first high-resolution far-infrared (far-IR) spectral survey of the Orion Kleinmann–Low (KL) region, we observed 20 CO emission lines with $J_{up} = 16$ to 39 (upper levels from $\approx$752 to 4294 K above the ground state). Observations were taken using the Long Wavelength Spectrometer on board the *Infrared Space Observatory* (*ISO*), in its high-resolution Fabry–Pérot (FP) mode ($\approx$33 km s^{-1}). We present here an analysis of the final calibrated CO data, performed with a more sophisticated modelling technique than hitherto, including a detailed analysis of the chemistry, and discuss similarities and differences with previous results. The inclusion of chemical modelling implies that atomic and molecular abundances are time predicted by the chemistry. This provides one of the main differences with previous studies in which chemical abundances needed to be assumed as initial condition. The chemistry of the region is studied by simulating the conditions of the different known components of the KL region: chemical models for a hot core, a plateau and a ridge are coupled with an accelerated Λ-iteration (ALI) radiative transfer model to predict line fluxes and profiles. We conclude that the CO transitions with $18 < J_{up} < 25$ mainly arise from a hot core of diameter 0.02 pc and a density of 10^7 cm^{-3} rather from the plateau as previous studies had indicated. The rest of the transitions originate from shocked gas in a region of diameter $\approx$0.06 pc with densities ranging from 3×10^5 to 1×10^6 cm^{-3}. The resulting CO fractional abundances are in the range $X(\mathrm{CO}) = (7.0–4.7) \times 10^{-5}$. A high-temperature post-shock region at more than 1000 K is necessary to reach transitions with $J_{up} > 32$, whilst transitions with $J_{up} < 18$ probably originate from the extended warm component. Finally, we discuss the spatial origin of the CO emission compared with that of the next most abundant species detected by the far-IR survey towards Orion KL: H_2O and OH.

Key words: line: identification – surveys – ISM: individual: Orion – ISM: lines and bands – ISM: molecules – infrared: ISM.

1 INTRODUCTION

At a distance of 450 pc, the Orion molecular cloud is the nearest massive star-forming region. Molecular emission mainly comes from the Orion Molecular cloud 1 (OMC1) which contains a number of infrared-emitting regions such as the Kleinmann–Low (KL) region (see the review by Genzel & Stutzki 1989). Since the first spectroscopic measurements in the millimetre, submillimetre and infrared (Storey et al. 1981; Genzel & Stutzki 1989; Sempere et al. 2000),

molecular emission has been shown to arise from several physically distinct regions (Irvine, Goldsmith & Hjalmarson 1987): the hot core, the compact ridge, the ridge, the plateau and the photodissociation region (PDR) surrounding the quiescent gas (see Fig. 1). The hot core and the plateau are characterized by elevated temperature due to star-forming activity (the hot core) or as consequence of outflows and shocks (the plateau), while the ridge represents extended, cooler and quiescent material.

The powerful molecular outflow associated with OMC1 was discovered by Zuckerman, Kuiper & Rodriguez (1976), being later noted as containing a weak bipolarity by Erickson et al. (1982),
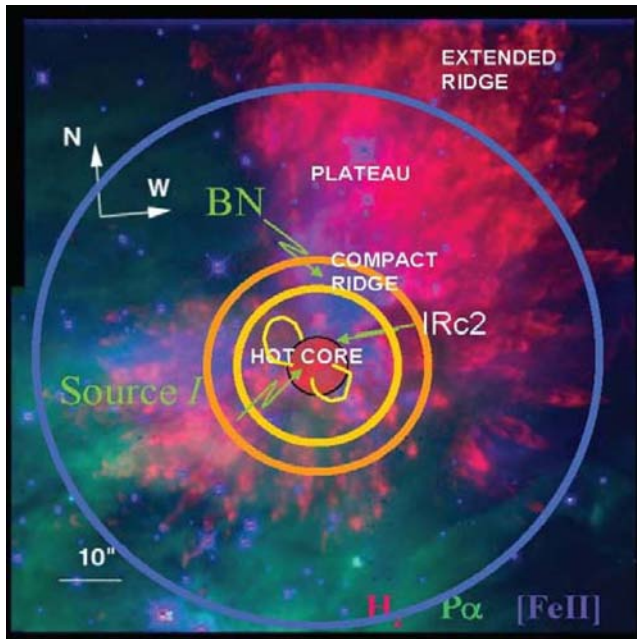
⋆E-mail: mercedes.ramos@deimos-space.com

Figure 1. The sketch of the different components in Orion KL overplotted on the image of Schultz et al. (1999). Colours correspond to the emission in H₂ (red), P_α (green) and [Fe II] (blue). Note that the large circle is the approximate size of the LWS beam.

and subsequently mapped with greater sensitivity and resolution. Recent observations have shown that the observed bipolar high-velocity outflow probably originates at the position of radio source I (Menten & Reid 1995; Gezari, Backman & Werner 1998; Chandler & Greenhill 2002). Source I is just 0.5 arcsec from IRc2, which had been believed to be the major source of the luminosity in the region ($L \approx 10^5$ L$_\odot$: Genzel & Stutzki 1989). The hot core is probably a dense clump, or a set of clumps, in the cavity surrounding these locations, with a gas kinetic temperature near 200 K. The main heating mechanism is radiative, warming up the grains and thus inducing thermal evaporation of their icy mantles (Goldsmith et al. 1983).

The Plateau emission comes from a mixture of outflows, shocks and interaction regions where shock chemistry may be dominant, being responsible for the large observed abundance of species such as SO, SO₂ and SiO. These species can be easily formed in the heated gas due to enhancements of the S, Si abundances following grain disruption in the shocked region and OH abundances through gas-phase reactions at high temperature. However, fragile molecules such as H₂CO or HDO have also been detected in the plateau, suggesting that small dense condensations may be present in the surrounding outflow (Blake et al. 1986). It is therefore difficult to discriminate between processes due to high-temperature gas-phase reactions or grain surface chemistry.

Interactions between the powerful outflow and quiescent ambient material are thought to give rise to the compact ridge emission, which is also referred to as the southern condensation. This emission region appears to be spatially compact, being revealed in observations of [C I] as a double-peaked structure from a shell of radius ≈20 arcsec (Pardo, Cernicharo & Phillips 2005). Finally, there is a surrounding layer of warm photodissociated material, arising from the non-ionizing ultraviolet (UV) radiation from the Trapezium OB stars (Rodriguez-Franco et al. 2001).

Among molecular tracers, CO is of particular interest because of its high abundance, and because observations of different transi-

tions can trace regions with significant differences in their physical properties. CO transitions with low-J_{up} values trace the less dense gas, with moderate temperatures and constituting the bulk of the outflow, while the highest J_{up} transitions trace either a dense or high-temperature gas.

The first Orion KL far-infrared (far-IR) CO line detection was by Watson et al. (1980), with the Kuiper Airborne Observatory (KAO). Their detections of the $J = 21 - 20$ and $22 - 21$ transitions, at 124 and 119 μm, indicated the presence of at least two different temperature components, with temperatures between 400 and 2000 K and a density in the range of $1–5 \times 10^6$ cm^{-3}. In a more recent analysis of *Infrared Space Observatory ISO* Long Wavelength Spectrometer (LWS) data, Sempere et al. (2000) concluded that the CO emission could be described by three temperature components in the plateau and ridge, with temperatures ranging from 300 to 2000 K and column densities of N(CO) $= 10^{17}–10^{19}$ cm^{-2}.

On the other hand, our far-IR survey of Orion KL (Lerate et al. 2006) showed the presence of P-Cygni line profiles in H₂O and OH transitions, revealing their outflow origin. Recent analyses of these transitions (Cernicharo et al. 2006; Goicoechea et al. 2006) inferred a beam-averaged gas temperature of ≈100–150 K; however, it is still not clear if these molecules form via high-temperature neutral–neutral reactions due to shocks or via desorption from grains. The complexity of the region and the large beam size of the *ISO* Long Wavelength Spectrometer(≈80 arcsec) complicate the spatial differentiation of the molecular emission.

In this paper, we report our analysis of the final *ISO* LWS–FP CO line detections from our recently published far-IR spectral survey of Orion KL. Observations of multiple CO lines with the same instrument are of great value, since all the lines have the same instrumental calibration and the same pointing. We used a new approach to modelling the CO emission, in which chemical simulations are carried out independently for each of the main known physical components in the region. The resulting chemical outputs are then coupled with non-local accelerated Λ-iteration (ALI) radiative transfer modelling in order to reproduce the observed line shapes and fluxes.

2 OBSERVATIONS AND DATA REDUCTION

The data set consists of 26 individual *ISO* observations in the LWS high-resolution modes L03 and L04. The complete list of Target Dedicated Time identification numbers (TDT's) and detailed description of the data processing can be found in Lerate et al. (2006). The angular and spectral resolution achieved across the LWS range was ≈80 arcsec and 33 km s^{-1}, although this could vary slightly depending on the LWS detector (Gry et al. 2003). Table 1 summarizes the detectors in which the different CO J transitions are observed and the effective aperture for this wavelength in arcsec. The last three columns are the instrumental resolving power, the full width at half-maximum (FWHM) of the resolution element and the overall calibration accuracy in μm (Swinyard et al. 1996). The velocity accuracy achieved for the LWS–FPs during the mission is quoted as 6 km s^{-1} for Fabry–Perot short (FPS) and 13 km s^{-1} for Fabry–Perot long (FPL) (Gry et al. 2003). However, it should be noted that this is only for the absolute velocity, i.e. comparing to an absolute standard of rest for an individual object, and arises primarily in the uncertainty in the knowledge of the absolute velocities of the sources used for the calibration of the instrument. For comparison of relative velocities of components within a given source, the better measure to take is the statistical error on the centroid found from repeated measurement of the same line on the same source over the

Table 1. *J* range of observed CO transitions for each detector and their effective radius aperture, resolving power and resolution element.

J range	FP	Detector	Effective aperture (arcsec)	Resolving power	Resolution element (μm)	rms accuracy
15–13	FPL	LW5	66.4	8500	0.0209	2.7×10^{-3}
18–16	FPL	LW4	69.4	8900	0.0180	2.7×10^{-3}
21–19	FPL	LW3	71.0	9250	0.0153	2.7×10^{-3}
25–21	FPL	LW2	77.8	9600	0.0127	2.7×10^{-3}
30–24	FPL	LW1	77.2	9700	0.0105	2.7×10^{-3}
34–29	FPL	SW5	79.0	9200	0.0092	2.7×10^{-3}
39–33	FPL	SW4	81.8	7800	0.0097	2.7×10^{-3}
45–38	FPS	SW3	87.0	8200	0.0081	8×10^{-4}
52–45	FPS	SW2	84.6	8450	0.0066	8×10^{-4}

course of the mission (ibid). For both FPs, we take this as ±5 km s^{-1} over all wavelengths.

Observations were centred at either RA J2000 05^{h}35^{m}14^s.12 Dec. (2000) – 05°22′22″.9 on at RA (J2000) 05^{h}35^{m}14^s.45 Dec. (J2000) – 05°22′30″.0, including both the BN object and IRc2 in the beam. The data processing were carried out using Offline Processing (OLP), the LWS interactive Analysis (LIA) package version 10 and the *ISO* Spectral Analysis Package (ISAP). Further processing was also carried out by including dark current optimization, deglitching and removal of the LWS grating residual profile (Lerate et al. 2006). A full grating spectrum with lower spectral resolution was also acquired but these data suffer from detector saturation effects. Thus, only the FP observations are considered in this work.

3 THE CHEMICAL AND RADIATIVE TRANSFER MODELS

The three main components in Orion KL (hot core, plateau and the ridge) were chemically modelled. The model is made from a two-stage calculation: in Stage I, the chemical evolution from diffuse gas to a dense core is computed. In Stage II, the chemical evolution of the plateau and ridge is investigated.

The time-dependent outputs from the chemical model are the fractional abundances of gas-phase and grain surface species. The fractional abundance of CO was then coupled with a radiative transfer model and line profiles and intensities directly compared with observations. The method and the models are similar to those used by Benedettini et al. (2006) to study the chemical structure of molecular clumps along chemically rich outflows. Each component is modelled independently. The final synthetic line spectrum is obtained by adding up the contribution of the three components.

3.1 The chemical models: the hot core, the plateau and the ridge

The hot-core model is described by Viti et al. (2004a). It is a modification of the model described by Viti & Williams (1999), where more detailed information about the molecules included and main reactions can be found. The model follows the chemical evolution of a free-fall collapsing cloud. The chemical evolution of the molecular species is then investigated after typical densities of hot cores (∼10^7 cm^{-3}) have been reached. The effect of an IR source is simulated by an increase in the gas and dust temperature (see Viti et al. 2004a, for more details). The initial and final densities of the collapsing core are 4×10^2 and 10^7 cm^{-3}. The diameter of the core is 10 arcsec (≈0.02 pc), as estimated by observations of hot cores (e.g. Blake et al. 1986) and the final visual extinction is ≈400 mag. During collapse, gas-phase species accrete, or freeze-out, on to the dust. The efficiency of accretion, f_r, is a free parameter and a grid of conditions for different f_r values was investigated, from $f_r = 0.03$–0.63 ($f_r = 1$ means 100 per cent efficiency). The best-fitting model was for $f_r = 0.23$, which led to 98 per cent of the CO in the form of ice at the end of Stage I.

The models used to simulate the plateau and ridge are described by Viti et al. (2004b). As in the hot-core model, we have a two-phase calculation, where the gravitational collapse occurs in Stage I. Both the ridge and the plateau components are believed to be affected by shocks due to the outflows activities. In Stage II, we therefore simulate the presence of non-dissociative shocks by an increase in temperature at an age of ≈1000 yr, corresponding to the dynamical time-scale of the main outflow observed in the KL region (Cernicharo et al. 2006). The efficiency of freeze-out during Stage I, the shock temperatures and the unshocked gas temperatures are free parameters and Table 2 lists the choice of these parameters for the

Table 2. List of Plateau and Ridge models and their parameters: density, maximum temperature reached by the gas in the shock simulation, gas temperature after cooling and the percentage of mantle CO (mco) given by the freeze-out parameter at the end of Stage I of the chemical model.

Model	Density (cm^{-3})	T_{shock} (K)	T_{gas} (K)	mco (per cent)	Model	Density (cm^{-3})	T_{shock} (K)	T_{gas} (K)	mco (per cent)
PL1	3×10^5	200	80	40	PL9	1×10^6	300	90	60
PL2	3×10^5	300	90	60	PL10	1×10^6	300	90	80
PL3	3×10^5	500	90	60	PL11	1×10^6	500	90	60
PL4	3×10^5	500	90	80	PL12	1×10^6	500	90	80
PL5	3×10^5	1000	100	60	PL13	1×10^6	1000	100	60
PL6	3×10^5	1000	100	80	PL14	1×10^6	1000	100	80
PL7	3×10^5	2000	100	60	PL15	1×10^6	2000	100	60
PL8	3×10^5	2000	100	80	PL16	1×10^6	2000	100	80
RG1	1×10^4	No shock	70	40	RG3	5×10^4	No shock	80	40
RG2	1×10^4	No shock	70	20	RG4	5×10^4	No shock	80	20

grid investigated. The parameters were chosen based on the results of previous studies of the Orion KL components (Blake et al. 1987; Genzel & Stutzki 1989).

3.2 The radiative transfer model

The chemical model produces abundances that are used as inputs to the radiative transfer model SMMOL (Rawlings & Yates 2001; van Zadelhoff et al. 2002), along with values for the scale, density, dust temperature and interstellar radiation field. The SMMOL code has ALI that solves the radiative transfer problem in multilevel non-local conditions. It starts by calculating the level population assuming LTE and the interstellar radiation field as input continuum and then recalculates the total radiation field and repeats the process until convergence is achieved. The resulting emergent intensity distribution is then transformed to the LWS units of flux (W cm^{-2} μm^{-1}) taking into account the different beam sizes (slightly different for each detector) and convolved with an instrumental line profile corresponding to a 33 km s^{-1} FWHM Lorentzian (Polehampton et al. 2007), in order to directly compare with the observations. The main input parameters include molecular data such as molecular mass, energy levels, radiative and collisional rates and also the dust size distribution and opacity. The CO molecular data were taken from molecular public data bases (Müller et al. 2001; Schöier et al. 2005). The input parameters also include the gas and dust temperatures of the object to model, such as the kinetic and dust thermal temperature.

We estimated the dust temperature from the LWS grating observation of Orion KL (Lerate et al. 2006), fitting a blackbody function of 80 K. The gas kinetic temperature is based on the chemical model input which varies for the different models considered (hot core, Plateau, PDR, see also Table 2). In order to reproduce the observed continuum flux level, we adopted a radiation field equivalent to 10^4 habings. This value is in agreement with previous continuum studies performed in the submillimetre which constrains the Interstellar Radiation Field (ISRF) enhancement to 10^3 to 10^4 times the standard ISRF (Jorgensen et al. 2006). The microturbulent velocity was set to 5 km s^{-1} and different expansion velocities from 15–40 km s^{-1} were also considered for the shocked gas in the Plateau models. We estimated an error of less than 30 per cent for the fit to the continuum, being the per cent deviation below the observed continuum for wavelengths up to 120 μm and above the observed continuum for the longest wavelengths.

4 RESULTS

Figs 2–4 show the chemical models that best fit our observations. The resulting model continuum is plotted in Fig. 5 along with the observed CO lines. The selection of species to be considered was based on the most abundant molecules detected in our far-IR survey towards Orion KL (i.e. CO, H$_2$O and OH). We used a χ^2 fit to compare model line profiles with observations. The modelled lines were rebinned to the same spectral sampling as the observations before the χ^2 fitting. Fig. 6 shows the best-fitting models compared to the observed CO lines. Table 3 shows the computed densities, temperatures and fractional abundances obtained for the different components. The contributions to the line fluxes and profiles from the different models described below were summed to give the total fluxes listed in Table 3 and the profiles shown in Fig. 6. Line peaks are also listed in column 4. Quoted errors are based on goodness of fit estimation and do not include calibration errors. The overall velocity error should include the calibration error of ±5 km s^{-1}
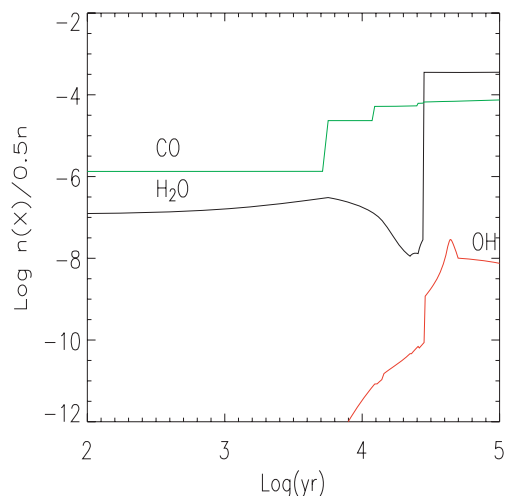

Figure 2. Time evolution of the abundances of CO, OH and H$_2$O in the hot-core model.

discussed in Section 2. The main results are listed in Table 4 and can be summarized as follows.

(i) CO transitions with $J_{up} < 18$ (i.e. lines at wavelengths >144.78 μm and upper energy levels E_{up} lower than ≈945 K) are best reproduced by a Plateau chemical model (PL2 in Table 1) with a density of 3×10^5 cm^{-3}, reaching a maximum temperature of 300 K. This could correspond to Plateau winds within the extended warm components. Ridge models with lower temperature and densities fail to reproduce these transitions.

(ii) CO transitions with $18 < J_{up} < 25$ (i.e. lines at wavelengths between 104.45 and 144.78 μm and with upper level energies between ≈1795 and 945 K) are best reproduced by a hot-core model with a mass of ≈25 M$_\odot$, a density of 1×10^7 cm^{-3} and a diameter of ≈0.020 pc.

(iii) Transitions with $30 > J_{up} > 25$ (i.e. lines between 87.19 and 104.45 μm, with upper level energies in the range 2567–1795 K) are best reproduced by a Plateau model (PL3) with a density of 3×10^5 cm^{-3}, simulating a shock that heats the gas to 500 K during a period of 100 yr at the age of 1000 yr.

(iv) Higher energy CO transitions, with $J_{up} > 30$, are best fitted by a Plateau model (PL14) with a higher density, 1×10^6 cm^{-3} and a freeze-out efficiency of 80 per cent, simulating a post-shock region at 1000 K which heats the gas, at an age of 1000 yr. All Plateau models had a diameter of ≈0.061 pc.

X(CO), the CO/H$_2$ fractional abundance, varies slightly as a function of cloud depth, from 7.0×10^{-5} to 4.7×10^{-5}, with an enhancement in the hot-core component. This is an effect of the different densities, and therefore freeze-out efficiencies.

5 DISCUSSION

5.1 The extended warm component

Our model results indicate that the lowest energy far-IR CO transitions originate from warm (≈300 K) and dense (≈10^5 cm^{-3}) gas. The derived temperature and density agree reasonably well with those from the combined flux ratios of [O I] 63.2/145.5 μm and [O I] 63.2/[C II] 157.7 μm which yielded a temperature of 300 K and a density of ≈10^5 cm^{-3} (Lerate et al. 2006).
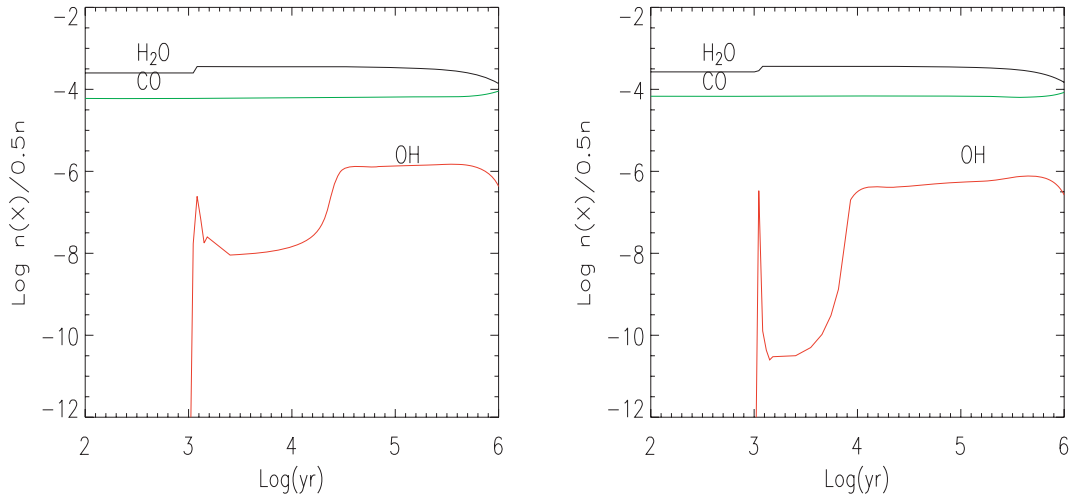
Figure 3. Plateau chemical models PL3 and PL14 (see Table 2) found to provide the best fit to the CO lines (see also Fig. 6).
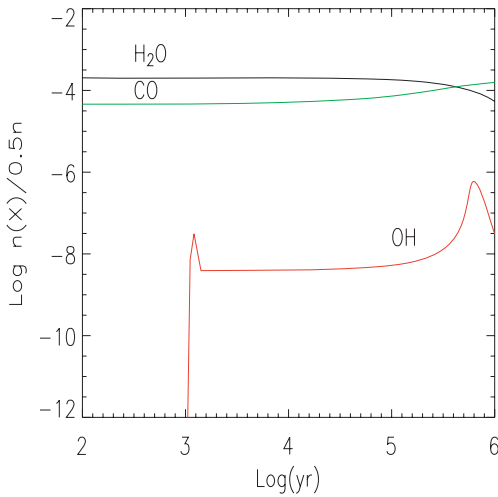

Figure 4. Model PL1, found to fit CO transitions with $J_{up} < 18$ (see also Fig. 6).

Figure 5. Model of the continuum adopted in the radiative transfer model.

The results agree with the gas density component described in Sempere et al. (2000) as the extended ridge emission with density of $\approx 10^5$ cm^{-3} and temperatures > 120 K. Similar results were found by Maret et al. (2001); however, they explained the emission as due to the non-ionizing ultraviolet (UV) radiation from the Trapezium stars, i.e. the PDR.

5.2 The plateau

The CO transitions with $18 < J_{up} < 30$ can be fitted by a two-component emission region. The low-velocity plateau is modelled by simulating a non-dissociative C-type shock of ≈ 30 km s^{-1} which leads to an increase in gas temperature to 1000 K in a period of ≈ 100 yr, reaching its maximum temperature at an age of 1000 yr, followed by fast cooling to temperatures of 100 K (as described by Bergin et al. 1998). The density and diameter of this region are 10^6 cm^{-3} and ≈ 0.061 pc, respectively, and this model component gives a good fit to the observed high-J CO transitions. Both Sempere et al. (2000) and Maret et al. (2001) agree on the presence of hot and dense gas arising from the shocked region at the interaction of the
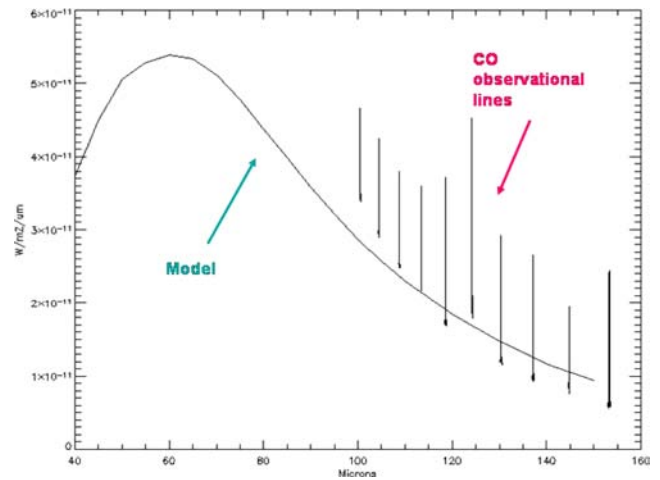
outflows with the ambient gas. However, their quoted temperatures (1500–2000 K) and densities (up to 3×10^7 cm^{-3}) are higher than implied by our models.

The CO transitions with $30 > J_{up} > 25$ are best fitted by a lower temperature shock model. Here, the maximum temperature is 500 K, with subsequent cooling down to 90 K. This result provides a new finding, being the first time that these transitions are associated with a low-temperature shock. Our interpretation is that this emitting region may be the external plateau, characterized by a density of 3×10^5 cm^{-3}, probably formed as consequence of the interaction of the many condensations in the flow (at lower velocity than in the inner part of the plateau) with the surrounding quiescent medium. Note, however, that Sempere et al. (2000) found that transitions with $18 < J_{up} < 33$ were best reproduced by a higher density component at 10^7 cm^{-3} and $T = 400$ K. A similar result is presented by Maret et al. (2001) which also includes transitions from $J_{up} = 20$–30. We found that in those intervals only transitions with $J_{up} > 25$ are emitted by the plateau, as the remainder is better reproduced by the hot-core model, consistent with the high density required by their models.
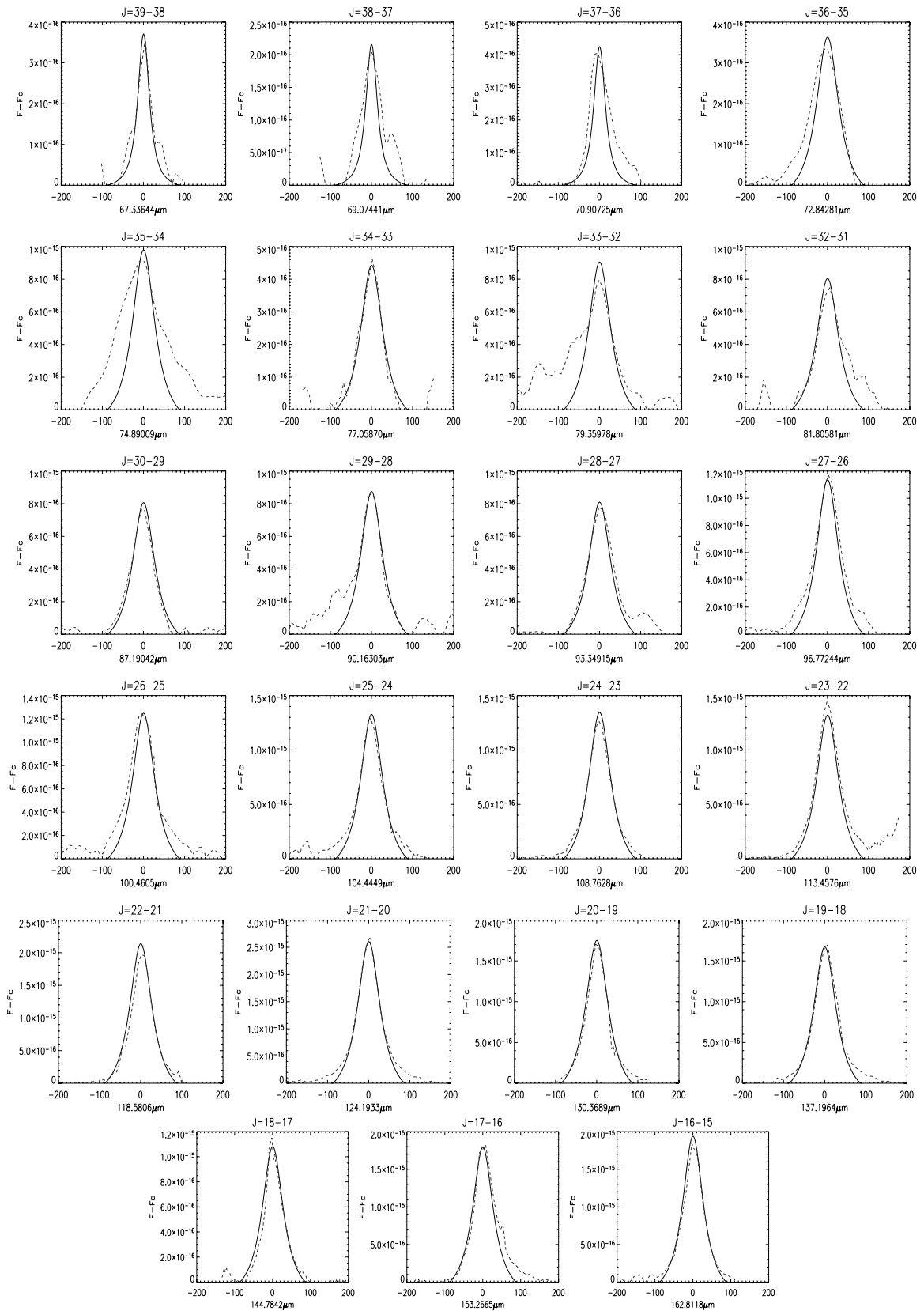
Figure 6. Line profiles from the radiative transfer models (solid lines) overplotted on the observed CO lines (dotted lines). The ordinate corresponds to the continuum-subtracted flux and the abscissa is the velocity in km s^{-1}. CO transitions with $18 < J_{up} < 25$ (i.e. from wavelengths 104.45 to 144.78 μm) are reproduced by the hot-core model. Transitions with $30 > J_{up} > 25$ (i.e. lines between 87.19 and 104.45 μm) are reproduced by the Plateau model PL3. CO transitions with $J_{up} > 32$ are reproduced by the Plateau model PL14 and transitions with $J_{up} < 18$ by model PL1 (see the text for a description of these models).

Table 3. CO line fluxes and summary of the main model parameters and results.

J	Flux (10^{-17} W cm^{-2})	Predicted flux (10^{-17} W cm^{-2})	Line peak (km s^{-1})	FWHM (km s^{-1})	Component Size (arcsec)	V_{LSR} (km s^{-1})	$[N(CO)/(H_2)]$ ($\times 10^{-5}$)	T_{max} (K)	Density (cm^{-3})
16–15	9.48 ± 0.26	9.62	12.7 ± 0.4	89.9 ± 11.5	50	9	4.66	300	1×10^5
17–16	8.66 ± 0.13	8.78	14.6 ± 0.2	75.2 ± 12.5	50	9	4.66	300	1×10^5
18–17	3.98 ± 0.26	4.08	15.5 ± 1.1	56.5 ± 11.2	50	9	4.66	300	1×10^5
19–18	5.22 ± 0.05	5.41	18.4 ± 0.2	55.4 ± 11.1	10	3–5	6.99	200	1×10^7
20–19	6.19 ± 0.22	6.08	16.1 ± 0.6	50.2 ± 10.9	10	3–5	6.99	200	1×10^7
21–20	7.89 ± 0.58	7.68	15.0 ± 1.1	50.5 ± 10.8	10	3–5	6.99	200	1×10^7
22–21	6.58 ± 0.09	6.49	12.5 ± 0.2	52.5 ± 10.9	10	3–5	6.99	200	1×10^7
23–22	4.82 ± 0.15	4.65	10.4 ± 6.3	53.2 ± 11.2	10	3–5	6.99	200	1×10^7
24–23	3.28 ± 0.12	3.20	9.7 ± 0.4	52.5 ± 10.8	10	3–5	6.99	200	1×10^7
25–24	3.67 ± 0.10	3.57	8.32 ± 0.2	56.6 ± 11.3	10	3–5	6.99	200	1×10^7
26–25	3.44 ± 0.06	3.31	11.5 ± 0.2	70.2 ± 11.6	10	3–5	6.99	200	1×10^7
27–26	3.82 ± 0.11	3.55	9.2 ± 0.3	70.1 ± 11.7	30	7–8	6.84	1000	1×10^6
28–27	1.89 ± 0.11	1.55	10.8 ± 0.6	68.5 ± 11.5	30	7–8	6.84	1000	1×10^6
29–28	1.58 ± 0.14	1.25	5.1 ± 0.4	90.2 ± 11.8	30	7–8	6.84	1000	1×10^6
30–29	1.58 ± 0.11	1.15	2.8 ± 0.2	57.5 ± 10.5	30	7–8	6.84	1000	1×10^6
32–31	1.52 ± 0.09	0.85	10.8 ± 0.6	79.5 ± 11.6	30	7–8	6.03	500	3×10^5
33–32	2.32 ± 0.20	0.81	3.7 ± 0.3	99.8 ± 12.1	30	7–8	6.03	500	3×10^5
34–33	0.60 ± 0.09	0.58	4.9 ± 0.7	66.6 ± 10.2	30	7–8	6.03	500	3×10^5
35–34	3.46 ± 0.40	0.78	0.1 ± 0.01	120.2 ± 15.5	30	7–8	6.03	500	3×10^5
36–35	0.62 ± 0.13	0.51	1.6 ± 0.3	80.2 ± 11.3	30	7–8	6.03	500	3×10^5
37–36	0.70 ± 0.06	0.59	10.1 ± 0.9	60.5 ± 11.5	30	7–8	6.03	500	3×10^5
38–37	0.45 ± 0.14	0.29	15.5 ± 4.8	56.6 ± 11.6	30	7–8	6.03	500	3×10^5
39–38	0.48 ± 0.14	0.31	12.4 ± 3.6	54.2 ± 11.9	30	7–8	6.03	500	3×10^5

Table 4. Summary of the main components and their physical parameters of size, density, gas temperature, dust temperature and per cent of mantle CO from the CO line modelling.

Component	Size (arcsec)	Density (cm^{-3})	T_{gas} (K)	T_{shock} (K)	mco (per cent)	CO J range
Extended warm gas	30	3×10^5	90	300	60	<18
Hot core	10	1×10^7	200		98	18–25
Plateau	30	3×10^5	90	500	60	25–30
Plateau	30	1×10^6	100	1000	80	>30

5.3 The hot core

The Orion hot core is well known to be warm ($T \approx 200$ K), compact (angular size $\approx$10 arcsec) and dense (10^7 cm^{-3}) (Blake et al. 1986; Wright et al. 1992). Such a hot core can reproduce well the CO fluxes and line profiles with $J_{up} = 18$–25. As mentioned in the plateau discussion, previous analyses of these transitions (Sempere et al. 2000; Maret et al. 2001) explain them as coming from the plateau where a high density and temperature $\approx$350–400 K component is needed to reproduce the lines. We find that this high-density component is in fact the hot core, where the temperature is close to 200 K. Plateau models of the same density and temperature fail to reproduce these transitions.

5.4 Velocity structure and the far-IR H$_2$O and OH lines

An analysis of the observed line radial velocities and their FWHMs can be used to distinguish emission originating from different components. However, the lack of spatial resolution complicates the analysis as the dynamical properties are diluted by the large LWS beam. The CO lines mainly peak in the LSR velocity range between +5 and 15 km s^{-1} (see Fig. 7); but because the line centre uncertainty is approximately ±5 km s^{-1}, it is difficult to establish whether lines originate from the plateau or from the hot-core component. Nevertheless, it seems clear that CO has a different spatial origin when compared to H$_2$O and OH molecules which have emission lines peaking in the range +20 and 40 km s^{-1} LSR and lines with pure absorption profiles, which peak at −10 to 20 km s^{-1}. Both the OH and H$_2$O emissions have been modelled (Cernicharo et al. 2006; Goicoechea et al. 2006) and it was inferred that they mainly arise from an extended flow of expanding gas at a velocity of $\approx$25 km s^{-1} with a density of $\approx$5 $\times$ 10^5 cm^{-3} and gas kinetic temperature of $\approx$100 K. The inferred beam-averaged abundances are $X(H_2O) = (2$–3$) \times 10^{-5}$ and $X(OH) = (0.5$–1$) \times 10^{-6}$ (Cernicharo et al. 2006; Goicoechea et al. 2006). These physical conditions are close to those found by our model of the plateau; however, we find that the water and OH abundances predicted by our chemical models are, respectively, higher and lower than those derived by Cernicharo et al and Goicoechea et al. from radiative transfer model of the observed lines (see Fig. 3).

For our models, the higher water abundance is due to (i) high efficiency in the hydrogenation of oxygen on the grains in Stage I, followed by evaporation of the icy mantles in Stage II and (ii) high-temperature reactions occurring during the shock phase (Elitzur & Watson 1978). The latter consist of
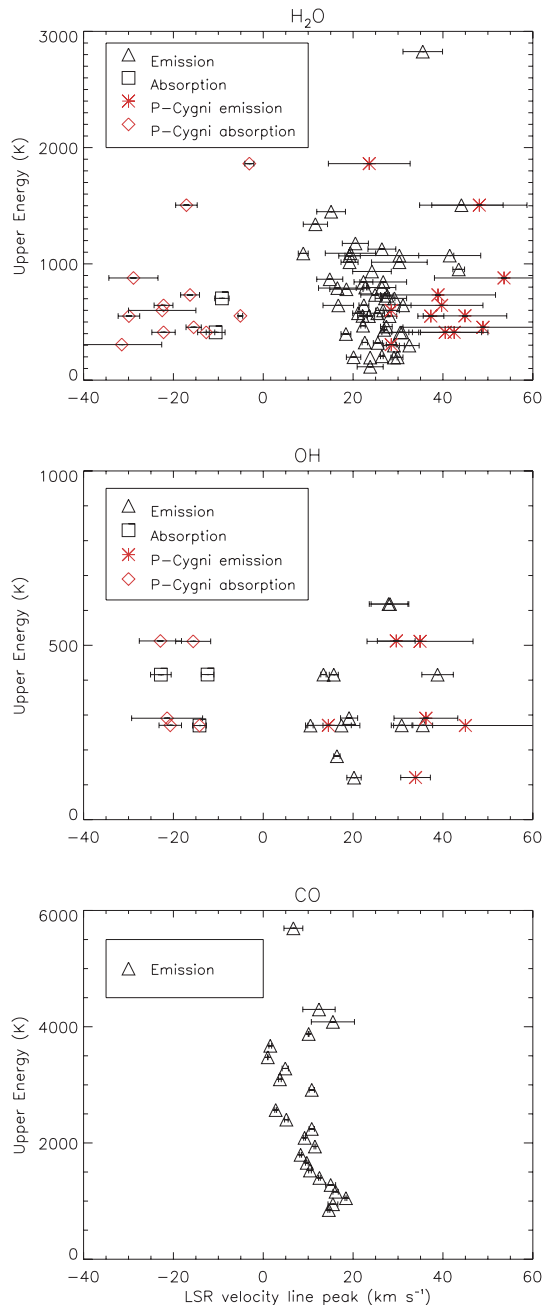
$$O + H_2 \rightarrow OH + H, \tag{1}$$

Figure 7. LSR peak velocities of H_2O, OH and CO lines observed towards Orion KL with the *ISO* LWS–FPs (Lerate et al. 2006). Note that only statistical errors are plotted and do not include the overall calibration uncertainty of ± 5 km s^{-1}.

$$OH + H_2 \rightarrow H_2O + H. \tag{2}$$

At higher temperatures, OH is also formed via molecular oxygen destruction:

$$O_2 + H_2 \rightarrow OH + OH. \tag{3}$$

The high temperatures produced by the shock are necessary to explain the OH abundance of $X(\text{OH}) = (0.5–1) \times 10^{-6}$. A shock temperature of at least 1000 K is required to reproduce the OH abundance. Possible explanations for the differences between the physical conditions inferred for the CO-emitting regions and those inferred for the H_2O- and OH-emitting regions include as follows.

(i) The latter two molecules arise from another physically distinct component, with no contribution from the hot core or the inner plateau.

(ii) The inferred H_2O and OH molecular abundances are, in fact, very diluted by the large LWS beam, where the contribution from shocked regions is not resolved. In this case, the use of a radiative transfer model alone is not enough to distinguish between the different components, and the resulting abundances may be locally underestimated.

6 CONCLUSIONS

We have analysed the final calibrated high-resolution *ISO* LWS–FP observations of CO lines using chemical models coupled with a non-local ALI radiative transfer model. The main physical parameters of the different components (density, temperature, scale, interstellar radiation field and dust temperature) are introduced in the chemical models together with physical parameters based on literature values for the hot core, plateau, ridge and the PDR surrounding the KL region. This technique allows a better approach to the difficult task of distinguishing between the emission from the different components included in the large ISO–LWS beam. Our modelling results show that CO transitions with $18 < J_{\text{up}} < 25$ are reproduced by a hot-core model of density $\approx 10^7$ cm^{-3} and a temperature of 200 K. This results suppose a new interpretation of the CO lines origin, as these transitions have been previously interpreted as originated in the Plateau component. Transitions between $25 < J_{\text{up}} < 39$ are reproduced by plateau models with densities ranging between 3×10^5 and 1×10^6 cm^{-3} simulating shocked material at 500–1000 K. Derived CO abundances are summarized in Table 3.

Our chemical models do not agree with the abundances previously found from the far-IR H_2O and OH emission lines (Cernicharo et al. 2006; Goicoechea et al. 2006). Therefore, we conclude that these species originate in a physically different region to that responsible for the CO emission. It is also possible that the inferred H_2O and OH abundances are underestimated due to the enhanced contributions from shocked components being diluted in the large LWS beam. This is because H_2O and OH emission lines were modelled by a different technique by the use of only a radiative transfer model, in which only one abundance for both species needed to be assumed.

We found the technique used here to be very efficient for understanding the chemistry and ideal for modelling high spectral and spatial resolution data. Future heterodyne instruments, such as HIFI on the ESA Herschel Space Observatory, with their much higher spatial and spectral resolution, will be better able to distinguish the different components in the complex region of Orion KL and, together with modelling techniques such as those developed here, should be capable of providing new insights into cloud chemical evolution during the process of massive star formation.

REFERENCES

Benedettini M., Yates J. A., Viti S., Codella C., 2006, MNRAS, 370, 229
Bergin E. A., Plume R., Williams P., Myers P. C., 1998, ApJ, 512, 724
Blake G. A., Sutton E. C., Masson C. R., Phillips T. G., 1986, ApJS, 60, 257
Blake G. A., Sutton E. C., Masson C. R., Phillips T. G., 1987, ApJ, 315, 621
Cernicharo J. et al., 2006, ApJ, 649, 33
Chandler C. J., Greenhill L. J., 2002, in Crowther P. A., ed., ASP Conf. Ser. Vol. 267, Hot Star Workshop III: The Earliest Stages of Massive Star Birth. Astron. Soc Pac., San Francisco, p. 357
Elitzur M., Watson W. D., 1978, A&A, 70, 443
Erickson N. R., Goldsmith P. F., Snell R. L., Berson R. L., Huguenin G. R., Ulich B. L., Lada C. J., 1982, ApJ, 261, 103
Genzel R., Stutzki J., 1989, A&A, 27, 41
Gezari D. Y., Backman D. E., Werner M. W., 1998, ApJ, 509, 283
Goicoechea J. R. et al., 2006, ApJ, 641, 49
Goldsmith P. F., Krotkov R., Snell R. L., Brown R. D., Godfrey P., 1983, ApJ, 274, 184
Gry C. et al., 2003, in Mueller T. G., Blommaert J. A. D. L., Garcia-Lario P., eds, ESA SP-1262, ISO Handbook Volume III (LWS). ESA Publications Division, Noordwijk
Irvine W. M., Goldsmith P. F., Hjalmarson A., 1987, in Hollenbach D. J., Thronson H. A., eds, Interstellar Processes. Reidel, Dordrecht, p. 561
Jorgensen J. K., Johnstone D., van Dishoeck E. F., Doty S. D., 2006, A&A, 449, 609
Lerate M. R. et al., 2006, MNRAS, 370, 59
Maret S., Caux E., Baluteau J.-P., Ceccarelli C., Gry C., Vastel C., 2001, in Pilbratt G. L., Cernicharo J., Heras A. M., Prusti T., Harris R., eds, ESA SP-460, The Promise of the Herschel Space Observatory. ESA Publications Division, Noordwijk, p. 455
Menten K. M., Reid M. J., 1995, ApJ, 445, L157
Molinari S., Brand J., Cesaroni R., Palla F., 2000, A&A, 355, 617
Müller H. S. P., Thorwirth S., Roth D. A. Winnewisser G., 2001, A&A, 370, 49
Pardo J. R., Cernicharo J., Phillips T. G., 2005, ApJ, 634, 61
Polehampton E. T., Baluteau J.-P., Swinyard B. M., Goicoechea J. R., Brown J. M., White G. J., Cernicharo J., Grundy T. W., 2007, MNRAS, 377, 1122
Rawlings J. M. C., Yates J. A., 2001, MNRAS, 326, 1423
Rodriguez-Franco A., Wilson T. L., Martin-Pintado J., Fuente A., 2001, ApJ, 559, 985
Schöier F. L., van der Tak F. F. S., van Dishoeck E. F., Black J. H., 2005, A&A, 432, 369
Schultz A., Colgan S., Erikson E., Kartman M., Hollenbach D., O'Dell C., Young E., Chen H., 1999, ApJ, 511, 282
Sempere M. J., Cernicharo J., Lefloch B., Gonzalez-Alfonso E., Leeks S., 2000, ApJ, 530, 123
Storey J. W. V., Watson D. M., Townes C. H., Haller E. E., Hansen W. L., 1981, ApJ, 247, 136
Swinyard B. M. et al., 1996, A&A, 315, L43
van Zadelhoff G. J. et al., 2002, A&A, 395, 373
Viti S., Williams D., 1999, MNRAS, 305, 755
Viti S., Codella C., Benedettini M., Bachiller R., 2004a, MNRAS, 350, 1029
Viti S., Collings M. P., Dever J. W., McCoustra R. S., Martin R. S., Williams D. A., 2004b, MNRAS, 354, 1141
Watson W. D., Storey J. W. V., Townes C. H., Haller E. E., Hansen W. L., 1980, ApJ, 239, 129
Wright M., Sandell G., Wilner C. J., Plambeck R. L., 1992, ApJ, 393, 225
Zuckerman B., Kuiper T. B. H., Rodriguez Kuiper E. N., 1976, ApJ, 209, 137

This paper has been typeset from a TEX/LATEX file prepared by the author.